2021

Molecular and Electronic Structures and Single-Molecule Magnet Behavior of Tris(thioether)-Iron Complexes Containing Redox-Active α-Diimine Ligands

Codrina V. Popescu
University of St. Thomas, Minnesota

Peng Wang

Mohamed R. Saber

Peter E. VanNatta

Glenn P. A. Yap

See next page for additional authors

Inorganic Chemistry

pubs.acs.org/IC Article

Molecular and Electronic Structures and Single-Molecule Magnet Behavior of Tris(thioether)−Iron Complexes Containing Redox-Active α-Diimine Ligands

Peng Wang, Mohamed R. Saber, Peter E. VanNatta, Glenn P. A. Yap, Codrina V. Popescu, Christopher C. Scarborough, Matthew T. Kieber-Emmons,* Kim R. Dunbar,* and Charles G. Riordan*

Cite This: *Inorg. Chem.* 2021, 60, 6480−6491 Read Online

ACCESS | Metrics & More | Article Recommendations | Supporting Information

ABSTRACT: Incorporating radical ligands into metal complexes is one of the emerging trends in the design of single-molecule magnets (SMMs). While significant effort has been expended to generate multinuclear transition metal-based SMMs with bridging radical ligands, less attention has been paid to mononuclear transition metal−radical SMMs. Herein, we describe the first α-diiminato radical-containing mononuclear transition metal SMM, namely, [κ^2-PhTt^{tBu}]-Fe(AdNCHCHNAd) (**1**), and its analogue [κ^2-PhTt^{tBu}]Fe-(CyNCHCHNCy) (**2**) (PhTt^{tBu} = phenyltris(*tert*-butylthiomethyl)-borate, Ad = adamantyl, and Cy = cyclohexyl). **1** and **2** feature nearly identical geometric and electronic structures, as shown by X-ray crystallography and electronic absorption spectroscopy. A more detailed description of the electronic structure of **1** was obtained through EPR and Mössbauer spectroscopies, SQUID magnetometry, and DFT, TD-DFT, and CAS calculations. **1** and **2** are best described as high-spin iron(II) complexes with antiferromagnetically coupled α-diiminato radical ligands. A strong magnetic exchange coupling between the iron(II) ion and the ligand radical was confirmed in **1**, with an estimated coupling constant $J < -250$ cm^{-1} ($J = -657$ cm^{-1}, DFT). Calibrated CAS calculations revealed that the ground-state Fe(II)−α-diiminato radical configuration has significant ionic contributions, which are weighted specifically toward the Fe(I)-neutral α-diimine species. Experimental data and theoretical calculations also suggest that **1** possesses an easy-axis anisotropy, with an axial zero-field splitting parameter D in the range from −4 to−1 cm^{-1}. Finally, dynamic magnetic studies show that **1** exhibits slow magnetic relaxation behavior with an energy barrier close to the theoretical maximum, 2|D|. These results demonstrate that incorporating strongly coupled α-diiminato radicals into mononuclear transition metal complexes can be an effective strategy to prepare SMMs.

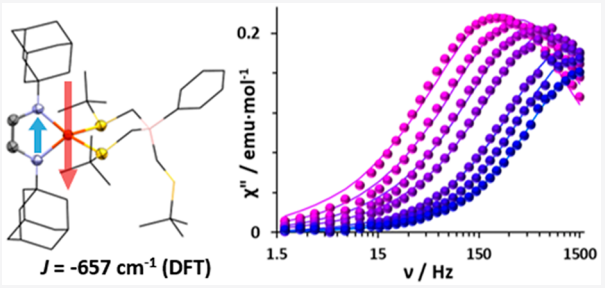

INTRODUCTION

Due to the modern development of advanced physical and computational methods, in-depth studies of the electronic structures of metal complexes have become increasingly tractable. Such studies are especially insightful for complexes with ambiguous electronic structure assignments due to noninnocent ligands that are bound to redox-active metals.[1−4] A survey of the recent literature reveals an increasing number of redox-active (noninnocent) ligand-containing metal complexes that exhibit interesting and new small-molecule activation and catalytic characteristics.[5−9] In addition, some redox-active ligand complexes have shown novel electronic and magnetic properties and thus the potential for use in applications such as spin-based molecular electronics and quantum computing devices.[10−16] In this context, a thorough understanding of their electronic structures through which structure−property and structure−reactivity relationships may be established is crucial for the rational design of catalysts and functional materials.

Over the past few years, several of our laboratories have been studying first-row transition metal complexes of redox-active 1,2-dioxolene ligands due to an interest in their bioinspired O_2 activity.[17−19] During our interrogation of the electronic structures of the dioxolene complexes, we discovered the magnetic bistability of several five-coordinate Co(II)-semiquinonate radical complexes.[20] These observations stimulated our interest in deducing the magnetic properties of the tris(thioether) ligand-containing transition metal complexes of redox-active ligands. Our attention was drawn to recent reports of radical-ligand-containing metal complexes that exhibit slow magnetic relaxation, a phenomenon characteristic of single-

Received: January 22, 2021
Published: April 12, 2021

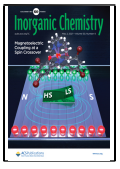

https://doi.org/10.1021/acs.inorgchem.1c00214
Inorg. Chem. 2021, 60, 6480−6491

molecule magnets (SMMs).[12] Due to potential applications in quantum information processing and high-density data storage, SMMs have received tremendous interest. Extraordinary effort has been put into synthesizing molecules with high spin-relaxation barriers. While the most recognized strategy to obtain SMMs focuses on maximizing the spin state (quantified as S) and the uniaxial magnetic anisotropy (quantified as the zero-field splitting parameter D), the design of the radical-ligand-containing SMMs takes into consideration a third parameter that has received less attention: the exchange coupling constant J. When radical ligands are incorporated into metal complexes, direct-exchange coupling involving paramagnetic metal ion(s) and radical ligand(s) is present. When the exchange coupling is sufficiently strong, i.e., the J value is large, the energy level of the spin ground state will be well below the energy levels of the excited states, resulting in a suppression of the relaxation pathways that involve spin excited states. Meanwhile, quantum tunneling processes within a single spin-state manifold might also be suppressed by the strong exchange coupling. Thus, incorporating the direct-exchange coupling of metal ions with radical ligands can be an effective strategy to produce SMMs with higher relaxation barriers.

In the pursuit of radical-ligand-containing SMMs, an emerging trend is to use strongly exchange-coupled redox-active bridging radicals to generate multinuclear transition metal-based SMMs.[12,21] This strategy has proven to be very effective and productive, generating diiron,[22−24] dicobalt,[25−30] and dinickel SMMs[25] with strong exchange couplings (in one example,[22] $|J| > 900$ cm^{-1}) and U_{eff} values up to 267(3) K[26] (U_{eff} is the effective spin-reversal barrier). A wide range of bridging radicals have been employed to construct these *dinuclear* transition metal-radical SMMs, including semiquinone radical,[25] tetraoxolene radical,[24] tetraazalene radical,[22,23] nindigo radical,[30] 2,2′-bipyrimidine radical,[28] tetrazine radical,[29] tetrapyridophenazine radical,[27] and 1,2,4,5-tetrakis(methanesulfonamido)benzene) radical ligands.[26] In contrast, *mononuclear* transition metal-radical SMMs have received less attention despite the rapid growth in the number of transition metal-based mononuclear SMMs.[31,32] Current examples of mononuclear transition metal-radical SMMs are limited to cobalt−nitroxide radical complexes,[33−35] cobalt−carbene radical complexes,[34−40] and an iron−dithiadiazolyl radical complex.[41] It is noteworthy that the magnitudes of the magnetic exchange interactions in these complexes are moderate (30 cm^{-1} < $|J|$ < 70 cm^{-1}).

Widely used in coordination chemistry and catalysis,[42−44] α-diimines are redox-active ligands that can access three different redox states: neutral α-diimines (L^0), monoanionic π-radicals (L^{-1}), and dianionic diamides (L^{-2}), where each state has distinct C−N and C−C bond distances (Scheme 1).[45] In addition, α-diimine ligands are easily accessible, and their steric and electronic properties may be tuned by varying the ligand substituents, i.e., R_1, R_2, and R_3 (Scheme 1). Most importantly, the monoanionic radical form of α-diimine ligands is well-known for delivering exceptionally strong exchange coupling,[15,16,46−48] making them attractive candidates for constructing mononuclear transition metal-radical SMMs. Notably, α-diiminato radical ligands (as well as the analogous iminopyridyl radical ligands) have recently been applied to construct mononuclear lanthanide-based SMMs.[49−52]

Scheme 1. Redox Series of α-Diimine Ligands: Neutral α-Diimines (L^0), Monoanionic π-Radicals (L^{-1}), and the Dianionic Diamide (L^{-2})[a]

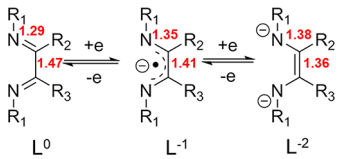

[a]Typical C−N and C−C bond distances (Å) for each state are labeled in red.

Herein, we report an α-diiminato radical-containing mononuclear iron complex, [κ^2-PhTt^{tBu}]Fe(AdNCHCHNAd) (**1**), that exhibits field-induced slow magnetic relaxation. We also report its analogue, [κ^2-PhTt^{tBu}]Fe(CyNCHCHNCy) (**2**). Both complexes were subjected to structural and spectroscopic characterizations and were found to have nearly indistinguishable geometric structures and spectroscopic features. The electronic structure and magnetic properties of **1** were further interrogated using a combined experimental and computational approach. The results indicate that **1** contains an antiferromagnetically coupled α-diiminato π-radical ligand with an exchange coupling constant $J < -250$ cm^{-1} ($J = -657$ cm^{-1}, DFT). To the best of our knowledge, the magnitude of the exchange coupling in **1** is among the largest observed in radical-containing SMMs. The calibrated computational studies also revealed that the ground state Fe(II)−α-diiminato radical configuration has a significant ionic character, which is weighted specifically toward the Fe(I)-neutral α-diimine description. To our knowledge, this unique electronic property has not been previously reported in any α-diimine-containing transition metal complex.

EXPERIMENTAL AND COMPUTATIONAL METHODS

2.1. General Information. All air- and moisture-sensitive reactions were performed under N_2 using standard Schlenk techniques or under an Ar or N_2 atmosphere in a Vacuum Atmospheres glovebox equipped with a gas purification system. Unless otherwise noted, all reagents were purchased from commercial sources and used without further purification. Solvents were of reagent-grade or better and were dried by passing them through activated alumina, then stored over 4 Å molecular sieves prior to use. Deuterated solvents were purchased from Cambridge Isotope Laboratories and stored over 4 Å molecular sieves. [PhTt^{tBu}]FeCl,[53] AdNCHCHNAd, and CyNCHCHNCy[54] were prepared following published procedures.

2.2. Synthesis of 1 and 2. *2.2.1. Synthesis of 1.* To the solution of [PhTt^{tBu}]FeCl (147 mg, 0.3 mmol) in 1 mL of THF and 30 mL of diethyl ether was added AdNCHCHNAd (97 mg, 0.3 mmol) in small portions. The reaction mixture was stirred for 1 h. A pink-purple precipitate formed. KC_8 (45 mg, 0.33 mmol) was then slowly added to the reaction mixture over about 10 min. The solution turned brown. After stirring for 3 h, the mixture was filtered through a pad of Celite, and the solvent was removed under vacuum. The residue was washed with pentane (2 × 4 mL), dissolved in 4 mL of benzene, and passed through a small plug of APTS-coated silica gel to remove impurities. After removing the benzene under vacuum, the residue was washed with pentane (2 × 2 mL) and dried under vacuum to obtain a yellow-brown powder (84 mg, 36%). Single crystals suitable for X-ray crystallography were obtained by the slow evaporation of the pentane/diethyl ether solution (v/v = 1:1) of the product at room temperature. ^{1}H NMR (C_6D_6): δ 126.2 (s, NC*H*), 31.3 (s, Ad), 29.7 (s, Ad), 8.8 (br, C(C*H*$_3$)$_3$S), 7.8 (s, (C$_6$*H*$_5$)B), 6.9 (s, (C$_6$*H*$_5$)B), 5.1 (s, Ad), 4.5 (s, Ad), 3.2 (s, C(C*H*$_3$)$_3$S (free)), 1.4 (s, Ad), −1.3 (s, C*H*$_2$S^{t}Bu), −11.2 (s, Ad), −11.5 (s, Ad). UV−Vis (THF): λ_{max} (ε, M^{-1} cm^{-1}) 289 (9748), 402 (7983), 456 (sh), 613 (380), 1007

https://doi.org/10.1021/acs.inorgchem.1c00214
Inorg. Chem. 2021, 60, 6480−6491

(188). LIFDI-MS: m/z calcd. for $C_{43}H_{70}BFeN_2S_3$ $(M)^+$ 777.4144, found $(M)^+$ 777.4152 (100%). μ_{eff} (C_6D_6) = 3.9(1) μ_B.

2.2.2. Synthesis of 2. To the solution of [PhTt^{tBu}]FeCl (147 mg, 0.3 mmol) in 8 mL of THF and 16 mL of diethyl ether was added CyNCHCHNCy (66 mg, 0.3 mmol) in small portions. The reaction mixture was stirred for 1 h. A dark blue solution was obtained. KC_8 (45 mg, 0.33 mmol) was then slowly added to the reaction mixture over about 10 min. The solution turned brown. After stirring for 3 h, the mixture was filtered through a pad of Celite, and the solvent was removed under vacuum. The residue was washed with pentane (2 × 4 mL), dissolved in 4 mL of benzene, and passed through a small plug of APTS-coated silica gel to remove impurities. After removing the benzene under vacuum, the residue was washed with pentane (2 × 2 mL) and dried under vacuum to obtain a yellow-brown powder (90 mg, 45%). Single crystals suitable for X-ray crystallography were obtained by the slow evaporation of a concentrated diethyl ether solution of the product at room temperature. ^{1}H NMR (C_6D_6): δ 139.5 (s, NC*H*), 29.1 (s, Cy), 27.0 (s, Cy), 8.9 (br, C(C*H*$_3$)$_3$S), 7.9 (s, (C$_6$*H*$_5$)B), 6.8 (s, (C$_6$*H*$_5$)B), 5.2 (s, Cy), 2.6 (s, C(C*H*$_3$)$_3$S (free)), −1.1 (s, C*H*$_2$S^{t}Bu), −8.5 (s, Cy), −9.9 (s, Cy). UV−Vis (THF): λ_{max} (ε, M^{-1} cm^{-1}) 294 (8400), 401 (6816), 458 (sh), 615 (285), 984 (195). LIFDI-MS: m/z calcd. for $C_{35}H_{62}BFeN_2S_3$ $(M)^+$ 673.3518, found $(M)^+$ 673.3542 (100%). μ_{eff} (C_6D_6) = 3.9(1) μ_B.

2.3. Physical Methods. NMR spectra were recorded on a Bruker AVIII 400 spectrometer. Chemical shifts (δ) were referenced to residual protons in the deuterated solvents. LIFDI-MS[55,56] was performed on a Waters GCT Premier mass spectrometer. Electronic absorption spectra were recorded on a Varian Cary 50 UV−vis spectrophotometer using screw-top quartz cuvettes with a 1 cm path length. Solution-state magnetic moments were determined using the Evans method.[57−59]

Continuous wave X-band EPR spectra were collected on a Bruker E580 at T = 10 K using a 0.2 mW (or 2 mW) power. The modulation amplitude was 10 G. EPR spectra were simulated in Matlab using EasySpin.[60]

Mössbauer spectra were recorded on a closed-cycle refrigerator spectrometer (model CCR4K) equipped with a 0.04 T permanent magnet while maintaining temperatures between 5 and 300 K. The samples consisted of solid powders (or crystalline material) that were suspended in Nujol, placed in Delrin 1.00 mL cups, and frozen in liquid nitrogen. The isomer shifts are quoted at 5 K with respect to the iron metal spectrum recorded at 298 K. Mössbauer spectra were analyzed using WMOSS software (Thomas Kent, See Co., Edina, MN).

The static magnetic properties of complex **1** were measured on samples of ground crystals using a Quantum Design MPMS-XL SQUID magnetometer operating over the temperature range 1.8−330 K at a 1000 Oe direct-current field. The data were corrected for diamagnetic contributions using Pascal constants. AC magnetic susceptibility measurements were performed on the same samples with an oscillating field of 5 Oe in the frequency range from 1 Hz to 1.5 kHz.

Single-crystal XRD data were obtained by mounting crystals onto plastic mesh using a viscous oil and cooling them to the data collection temperature. Data were collected on a Bruker-AXS APEX II CCD diffractometer with graphite-monochromated Mo Kα radiation (λ = 0.71073 Å). Unit cell parameters were obtained from 36 data frames, 0.3° ω, from three different sections of the Ewald sphere. The data sets were treated with absorption corrections based on redundant multiscan data. For **1**, the systematic absences in the diffraction data are consistent with the triclinic space group, $P\bar{1}$. For **2**, the systematic absences in the diffraction data are consistent with the monoclinic space group, $P2_1/c$, and the asymmetric unit contains two symmetry-independent molecules. All non-hydrogen atoms were refined with anisotropic displacement parameters. All hydrogen atoms were treated as idealized contributions. Atomic scattering factors are contained in the SHELXL 2013−2014 program libraries. The CIF filess have been deposited with the Cambridge Crystallographic Database as CCDC 1974684 for **1** and 1974685 for **2**.

2.4. Computational Methods. Initial density functional theory (DFT) calculations were performed in *Gaussian 16* rev. C.01.[61] A model of **1** was built from crystallographic coordinates and optimized using the BP86 functional[62,63] with definition two of Ahlrich's triple-ζ with polarization (def2-TZVP) basis[64] on all atoms in the gas phase on the broken symmetry S = 3/2 surface. An analytical frequency calculation was performed to ensure that a stationary point on the potential-energy surface had been reached and provide thermal corrections to the Gibbs free energy. No imaginary frequencies were obtained. Molecular orbitals were visualized with *Lumo*.[65]

A truncated model of **1** called **1*** was built using the optimized coordinates of **1** by replacing the phenyl ring with a hydrogen, replacing the noncoordinated thioether arm at the S position with a proton, and replacing the adamantane with a methyl that had the C located at the bridgehead carbon position. This truncated model was partially optimized by freezing the positions of the heavy atoms and allowing the hydrogens to freely optimize with the BP86 functional on the broken-symmetry S = 3/2 spin surface. Time-dependent (TD) DFT calculations were performed with the TPSSh functional with the polarizable continuum model in THF to yield the first 200 excited states.

The truncated model **1*** was subsequently used for property calculations in ORCA ver. 4.2.1.[66,67] All calculations used the same basis sets as above. A broken-symmetry DFT solution was initially computed and equivalent to the Gaussian computation. The fractional orbital occupation density (FOD) was computed on both **1** and **1***.[68] Graphical FOD plots were generated from the electron density to define the delocalization of correlated electrons. Mössbauer parameters were calculated by determining the field gradient (V) and the electron density at the nucleus (ρ_0). The value of δ_{iso} was derived using ρ_0 and the TZVP correction parameters α, β, and C for the TPSSh functional[69] by $\delta_{iso} = \alpha(\rho_0 - C) + \beta$. EPR parameters were calculated using the gauge invariant origin. The D tensor was calculated by including spin−spin and spin−orbit contributions. The spin−orbit component included the 1e$^-$ terms, semi-numerical Coulomb terms, and exchange via one-center exact integrals.

The DFT broken-symmetry S = 3/2 model was used as an initial guess for a second-order Møller−Plesset perturbation theory (MP2) single-point calculation.[70] This calculation was subsequently used as the initial guess for a domain-based local pair-natural orbital (DLPNO) coupled-cluster (CC) calculation.[71,72] The CC calculation included single and double excitations and perturbative triples (CCSD(T)). CCSD(T) single-point calculations were performed on both the quartet and sextet states. The electric field gradient for the Mössbauer parameters was calculated analogously to that described above. Electron paramagnetic resonance properties were computed analogously to that described above, except the origin was defined as the center of charge and the resolution of the identity (RI) approximation[73] was used with associated auxiliary basis sets.

The DFT broken-symmetry S = 3/2 model was used to generate quasi-restricted orbitals (QRO) as the initial guess for complete active-space self-consistent field (CASSCF) computations. Preliminary CASSCF calculations were converged using a smaller basis set (def2-SVP), followed by a tighter convergence with the full basis as described above. These preliminary calculations employed the iterative-configuration expansion (ICE-SCF)[74] to dramatically speed up the computations. Orbitals were selected for inclusion in the active space using occupation number N (0.005 > N > 1.995). The final CASSCF calculations employed 11 electrons in 14 orbitals (CAS-(11,14)) utilizing the same basis sets as those in the DFT and CCSD(T) calculations. These calculations also required RI and appropriate auxiliary basis sets. Roots for state-averaged (SA) CASSCF were determined by an initial computation with frozen orbitals. Quartet and sextet roots within 10 000 cm^{-1} of the ground state were chosen for the SA-CASSCF. n-Electron valence second order perturbation theory (NEVPT2)[75] was used to determine the dynamic correlation energy correction to the ground-state CAS solutions, and the RI approximation was used. The strongly contracted (SC) variant of this method was used. Mössbauer

https://doi.org/10.1021/acs.inorgchem.1c00214
Inorg. Chem. 2021, 60, 6480−6491

parameters were calculated analogously to the CC computations, and the EPR parameters were calculated within the CASSCF module.

RESULTS AND DISCUSSION

3.1. Syntheses and Crystal Structures. Complexes **1** and **2** were synthesized in 36% and 45% yields, respectively, by the addition of 1 equiv of potassium graphite (KC_8) to a 1:1 mixture of [PhTt^{tBu}]FeCl and the corresponding α-diimine in THF/diethyl ether (Scheme 2). Yellow-brown crystals suitable

Scheme 2. Synthesis of 1 (R = Ad) and 2 (R = Cy)

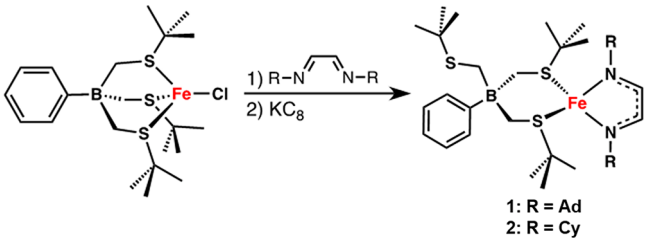

for X-ray diffraction were obtained for **1** and **2** by the slow evaporation of concentrated pentane/diethyl ether and diethyl ether solutions, respectively. Thermal ellipsoid plots of the molecular structures and selected metric parameters of **1** and **2** are shown in Figure 1. Complex **2** crystallizes with two symmetry-independent molecules, **2-Fe1** and **2-Fe2**, and only **2-Fe1** is shown in Figure 1. Both **1** and **2** contain a pseudotetrahedral iron center coordinated by two thioether sulfur atoms and two nitrogen atoms from the α-diimine ligand. The third sulfur is uncoordinated, likely due to the steric bulk of the R groups. The κ^2-coordination mode of the tris(thioether) ligand was also found in a dialkyltetraazadiene iron complex, namely [κ^2-PhTt^{tBu}]Fe(AdNNNNAd),[53] which is an isoelectronic analogue of **1** and **2**.

The average Fe–S distances in **1**, **2-Fe1**, and **2-Fe2** are 2.325(1), 2.327(1), and 2.331 (1) Å, respectively. These nearly indistinguishable distances suggest that the electron densities on the iron centers are very similar. Comparable Fe–S distances are found in [κ^2-PhTt^{tBu}]Fe(AdNNNNAd) (average Fe–S distance of 2.299(1) Å) as well as a four-coordinate high-spin (S = 3/2) iron(I) complex, [PhTt^{tBu}]Fe(PEt_3) (average Fe–S distance of 2.343(1) Å).[53] The average Fe–N distances are 1.974(2) Å for **1**, 1.970(2) Å for **2-Fe1**, and 1.976(2) Å for **2-Fe2**, indicating that different alkyl groups on the α-diimine ligands do not impart a difference in the geometric and electronic structures of **1** and **2**. Comparable Fe–N distances are also found in [κ^2-PhTt^{tBu}]Fe(AdNNNNAd)(average Fe–N distance of 1.945(3) Å).[53] Additionally, the Fe–N distances in **1** and **2** are very close to those of [ArNC(Me)C(Me)NAr)Fe]$_2$(μ-Cl)$_2$(Ar = 2,6-diisopropylphenyl) (average Fe–N distance of 1.979(1) Å), which is a high-spin diferrous complex with two α-diiminato π-radicals.[45,76]

The metric parameters that are most indicative of the redox state assignment of the α-diimine ligands are the C–N and C–C bond distances within the α-diimine moiety (Scheme 1).[45] Using the numbers shown in Scheme 1 as benchmarks, the average C–N bond lengths of 1.334(2) Å for **1**, 1.341(4) Å for **2-Fe1**, and 1.338(4) Å for **2-Fe2** are consistent with an α-diiminato π-radical monoanion description. In addition, the nearly identical C–C bond lengths of 1.395(3) Å for **1**, 1.395(4) Å for **2-Fe1**, and 1.391(5) Å for **2-Fe2** also support this assignment. Taking the metric parameters and charge balancing into consideration, **1** and **2** are best described as iron(II) complexes with α-diiminato π-radical ligands.

3.2. Spectroscopic and Static Magnetic Properties. In addition to their metric parameters, **1** and **2** share striking similarities in their electronic absorption spectra (Figure 2), which point to a common electronic structure. While the detailed assignments of the electronic transitions will be discussed later, it is informative to compare **1** and **2** with [iPrNC(Ph)CHNiPr]$_2$Fe, an iron(II) complex containing α-diiminato radical ligands, and [iPrNC(Ph)CHNiPr]$FeCl_2$, an iron(II) complex containing a neutral α-diimine ligand.[45] **1** exhibits strong charge-transfer (CT) transitions at 402 (7983 M^{-1} cm^{-1}) and 456 (sh) nm, and **2** exhibits similar CT bands at 401 (6816) and 458 (sh) nm. While analogous CT transitions in the 400–500 nm region, i.e., 441 (6000 M^{-1} cm^{-1}) and 515 nm (2000), were also observed for [iPrNC(Ph)CHNiPr]$_2$Fe, [iPrNC(Ph)CHNiPr]$FeCl_2$ lacks intense CT bands in the same region. Thus, the CT bands in the 400–500 nm region are suggestive of an α-diiminato radical ligand.

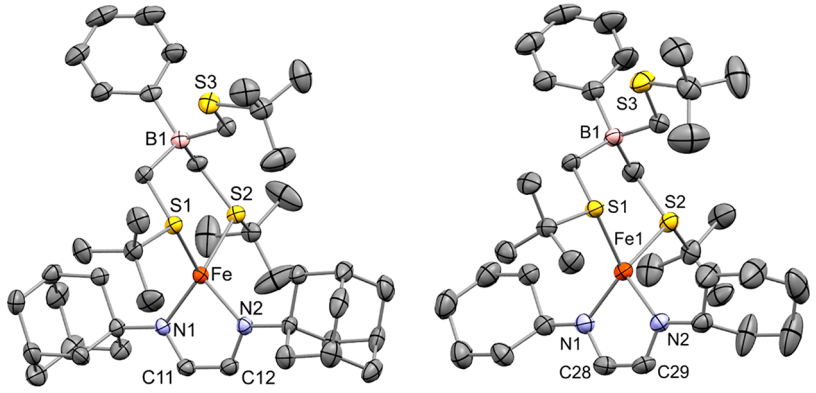

Figure 1. Molecular structure of **1** (left) and **2** (right, only **2-Fe1** is shown) with heteroatom labeling. Thermal ellipsoids are drawn to 30% probability. Hydrogen atoms have been omitted for clarity. Selected bond distances (Å) for **1** are as follows: Fe–S1 2.316(1), Fe–S2 2.334(1), Fe–N1 1.971(2), Fe–N2 1.976(2), N1–C11 1.336(2), N2–C12 1.332(2), and C11–C12 1.395(3). Selected bond distances (Å) for **2-Fe1** are as follows: Fe1–S1 2.327(1), Fe1–S2 2.327(1), Fe1–N1 1.970(2), Fe1–N2 1.969(2), N1–C28 1.342(4), N2–C29 1.339(4), C28–C29 1.395(4). Selected bond distances (Å) for **2-Fe2** are as follows: Fe2–S4 2.331(1), Fe2–S5 2.332(1), Fe2–N3 1.973(2), Fe2–N4 1.978(2), N3–C63 1.340(4), N4–C64 1.336(4), and C63–C64 1.391(5).

https://doi.org/10.1021/acs.inorgchem.1c00214
Inorg. Chem. 2021, 60, 6480–6491

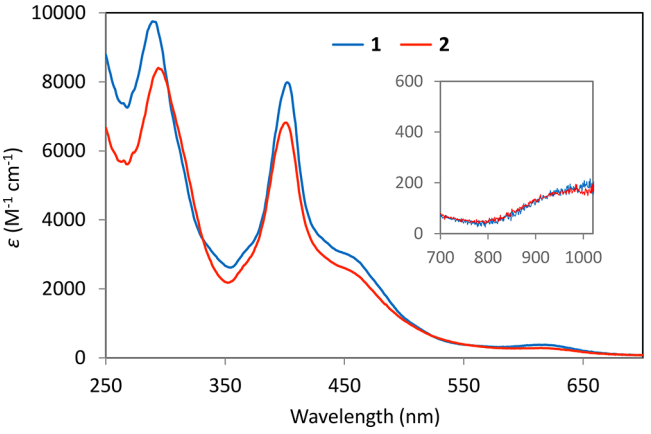

Figure 2. Electronic absorption spectra of [κ^2-PhTt^{tBu}]Fe(AdNCHCHNAd) (**1**, blue) and [κ^2-PhTt^{tBu}]Fe(CyNCHCHNCy) (**2**, red) in THF.

Given that **1** and **2** share a common electronic structure, only complex **1**, whose pure crystalline form was more readily obtainable in sufficient quantities, was subjected to further spectroscopic and magnetic property interrogations. While the C−N and C−C bond lengths are informative of the redox states of the α-diimine ligands, ^{57}Fe Mössbauer spectroscopy provides insight into the oxidation and spin states of the iron center. Figure 3 shows the Mössbauer spectrum of **1** at 80 K in a magnetic field of 0.04 T. Table S2 contains the Mössbauer parameters of **1** and other relevant iron complexes for comparison.

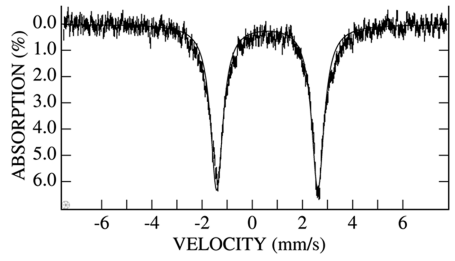

Figure 3. Mössbauer spectrum of a solid microcrystalline sample of **1** in Nujol at 80 K in a magnetic field of 0.04 T. The hashed lines represent the raw data, and the solid line is a result of the least-squares fit of the data.

1 exhibited an isomer shift at δ 0.60 mm/s and quadrupole splitting ΔE_Q = −4.03 mm/s (Table S2). The isomer shift of **1** is much larger than those of the all the S- and N,S-ligated iron(III) compounds in the literature (one example[77] is given in Table S2) but somewhat closer to those of the the high-spin iron(II) dimer {[PhTt^{tBu}]FeCl}$_2$ (δ 0.96(3) mm/s, Table S2)[53] and a bis(benzimidazolato) ligated diferrous [2Fe-2S] cluster (δ 0.79 mm/s, Table S2).[78] Interestingly, some sulfur-ligated high-spin Fe(I) complexes such as [PhTt^{tBu}]Fe(PMe$_3$) and [PhTt^{tBu}]Fe(PhCCPh) also exhibit similar isomer shifts (Table S2).[53] Nevertheless, when the Mössbauer data were considered with the crystallographic and electron absorption spectroscopic data, it is clear that **1** is most consistent with the description of a high-spin iron(II) complex with an α-diiminato radical ligand.

To study the magnetic interaction between the high-spin iron(II) and the α-diiminato radical ligand, static magnetic properties were measured on samples of crushed crystals of **1**. The data were corrected for the diamagnetic contribution using Pascal constants. As shown in Figure 4, the χT value of 1.91 cm^3·K/mol at 300 K (μ_{eff} = 3.91 μ_B) comports with the solution magnetic moment at room temperature, μ_{eff} = 3.9(1) μ_B, and corresponds to an S = 3/2 ground state (spin-only, g = 2.02) derived from the antiferromagnetic coupling between the high spin iron(II) center (S = 2) and the ligand radical (S = 1/2). The χT values remain nearly constant throughout the temperature range 25−300 K, indicating very strong magnetic-exchange coupling. Below 25 K, the χT values dropped gradually to 1.38 cm^3·K/mol^{-1} at 2 K, which may be attributed to zero-field splitting (ZFS) or intermolecular interactions. The field-dependent magnetization data collected at 1.8 K slowly increased at lower fields (Figure S1), which is indicative of antiferromagnetic intermolecular interactions. At fields above 5 T, the magnetization approaches saturation at 2.24 μ_B, which is well below the expected value for the S = 3/2 ground state and is also indicative of ZFS or intermolecular interactions. The field-dependent magnetization curves at different temperatures (1.8−4.5 K) are nonsuperimposable (Figure 4 inset), which is further indicative of ZFS. In order to obtain an acceptable estimation of the magnitude of the coupling constant J, the susceptibility data were simulated using *PHI* software[79] under the Hamiltonian

$$H = \mu BH(\boldsymbol{g}S_1 + \boldsymbol{g}S_2) + (S_1 \cdot \boldsymbol{D}_{ion} \cdot S_1) - 2J(S_1 \cdot S_2) \quad (1)$$

The first term corresponds to Zeeman splitting, whereas the second and third terms are the zero-field splitting in the metal ion and Heisenberg−Dirac−van Vleck magnetic exchange, respectively, where S_1 is the metal spin (S = 2) and S_2 is the radical spin (S = 1/2). Satisfactory simulations were obtained for coupling constant J values < −250 cm^{-1} (Figure 4). Simultaneous fitting of χT and the reduced magnetization data using the Hamiltonian in eq 1 resulted in $|D_{ion}|(E)$ = 2.24 (0.55) cm^{-1} with J = −660 cm^{-1} (g_1 = 2.19, g_2 = 1.94, and g_3 = 1.84). Notably, a similar tetrahedral iron(II)−radical complex also exhibits very strong antiferromagnetic coupling, which leads to an effective S = 3/2 ground state (LMeFe(AdNNNNAd), L = HC[C(Me)N(2,6-iPr2C$_6$H$_3$)]$_2$, J = −850 cm^{-1}).[80] Alternatively, the system was treated as a fully coupled S = 3/2 system, and the data were fit according to the Hamiltonian

$$H = \mu BH\boldsymbol{g}S_T + (S_T \cdot \boldsymbol{D}_T \cdot S_T) \quad (2)$$

Where S_T is the fully coupled 3/2 spin state resulted in $D_T(E)$ = −3.52 (−1.2) cm^{-1} (g_{av} = 1.99 given g_1 = 2.19, g_2 = 1.94, and g_3 = 1.84, EPR).

While static magnetometry measurements were used to estimate the ZFS parameters, this technique could not unequivocally determine the sign of the axial ZFS parameter D (i.e., D_T in eq 2). In this context, continuous-wave X-band EPR spectroscopy was performed to provide a high-resolution evaluation of the electronic structure of **1** (Figure 5). Experiments were conducted on dilute solutions (1 mM) in THF at 10 K at 2.0 and 0.2 mW power levels. The spectra are dominated by broad effective S = 1/2 features with effective g-values of 4.83, 3.27, and 1.92, which are consistent with high-spin iron. Given the model of a high-spin iron(II) strongly antiferromagnetically coupled to a α-diiminato ligand radical that developed above ($|J|$ > 250 cm^{-1}, Figure 4), the spectrum of **1** was modeled in a $J \gg D$ regime as an effective S = 3/2 system, meaning that the shape of the spectrum is dominated by ZFS. Consequently, fits to both positive and negative D

https://doi.org/10.1021/acs.inorgchem.1c00214
Inorg. Chem. 2021, 60, 6480−6491

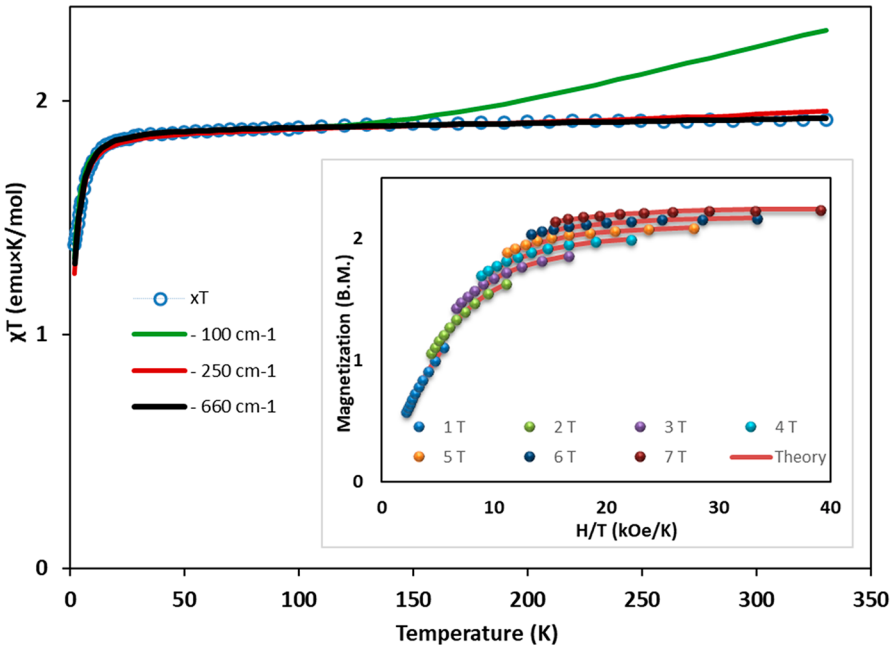

Figure 4. χT versus T plots (blue circles) for **1**. Simulations were done using *PHI* software[79] ($J = -100$ cm^{-1}, green; $J = -250$ cm^{-1}, red; and $J = -600$ cm^{-1}, black), where $|D_{ion}|$ (E) = 2.24 (0.55) cm^{-1}. The inset shows variable temperature field-dependent magnetization data for **1** at 1.8−4.5 K.

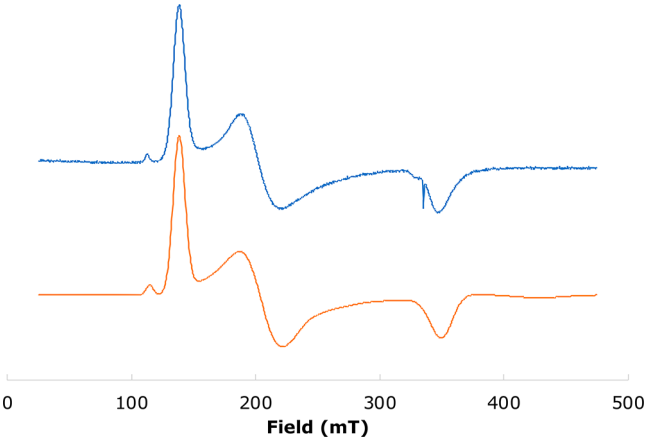

Figure 5. X-Band EPR spectrum of **1** at 10 K (9.3766 GHz, 10 G modulation amplitude, and 2 mW) (blue) and effective $S = 3/2$ fit (orange) with g = 2.19, 1.94, 1.84; $D = -2.65$ cm^{-1}; and E/D = 0.073.

were explored, which yielded the following two equivalently good fits: (i) g = 2.11, 2.04, and 2.02 (g_{av} = 2.06); D = +2.19 cm^{-1}; and E/D = 0.146 (Figure S5); and (ii) g = 2.19, 1.94, and 1.84 (g_{av} = 1.99); $D = -2.65$ cm^{-1}; and E/D = 0.073 (Figure 5). While these fits are indistinguishable, no satisfactory fit of the static magnetometry data can be accomplished with $g_{av} > 2.02$, suggesting that the latter fit with a negative D value is more consistent with the magnetometry experiments. In addition, computational studies with various methods further suggest that the sign of D is negative (vide infra).

3.3. Dynamic Magnetic Properties. Recently, metal−radical complexes have been extensively pursued as a viable route for improved magnetically coupled systems with SMM behavior.[12,21] In **1**, the strong exchange coupling between the α-diiminato radical and the high-spin iron(II) leads to an effective $S = 3/2$ magnetic center in an axially distorted tetrahedral coordination environment, which is typically expected to give rise to SMM behavior.[81,82] The large magnitude of the exchange coupling constant, $|J| > 250$ cm^{-1}, ensures a large separation between the low-lying spin excited states and the ground state. Such a large separation of the excited states is expected to eliminate a possible fast relaxation pathway that could otherwise be detrimental to the thermal energy barrier. In addition, strongly coupled radical discrete molecules were shown to exhibit a significant enhancement of the thermal relaxation barriers up to the theoretical maximum due to the suppression of quantum tunneling pathways.[26] Thus, despite of the relatively small easy-axis anisotropy (-4 cm^{-1} < D < 0), a small effective energy barrier to the spin reversal was expected (maximum relaxation barrier $U = (S^2 - 1/4)\,|D|$ for half-integer spin systems when $S = 3/2$ and $U = 2|D|$). Indeed, the AC susceptibility measurements of compound **1** revealed a field-induced out-of-phase AC signal up to 2.5 K, as shown in Figure 6, which is indicative of possible SMM behavior. To determine the optimum applied DC field, the frequency-dependent AC measurements of **1** were scanned under different applied DC fields to give the best signal under 1000 Oe (Figure S2). The frequency-dependent measurements at different temperatures in the range of ν (1−1500 Hz) were measured for the pure sample over the temperature range 1.8−2.5 K under a 1000 Oe DC field (Figure 7). The data were fit using a Debye model[83] to give an estimated energy barrier $U_{eff} = 5.3$ cm^{-1} and a pre-exponential factor $\tau_0 = 7.5 \times 10^{-6}$ s (1000 Oe) (Figure S3). Notably, the effective relaxation barrier exactly matches the theoretical maximum barrier, $U = 2|D|$ ($|D| = 2.65$ cm^{-1}, EPR). Thus, these results demonstrate the potential for using strongly exchange-coupled nonbridging radical ligands to achieve slow magnetic relaxation in mononuclear transition metal complexes even when the magnetic anisotropy is relatively small. While a number of mononuclear iron complexes, including iron(I),[84,85] iron(II),[86−95] and iron(III) complexes,[96−98] have

https://doi.org/10.1021/acs.inorgchem.1c00214
Inorg. Chem. 2021, 60, 6480−6491

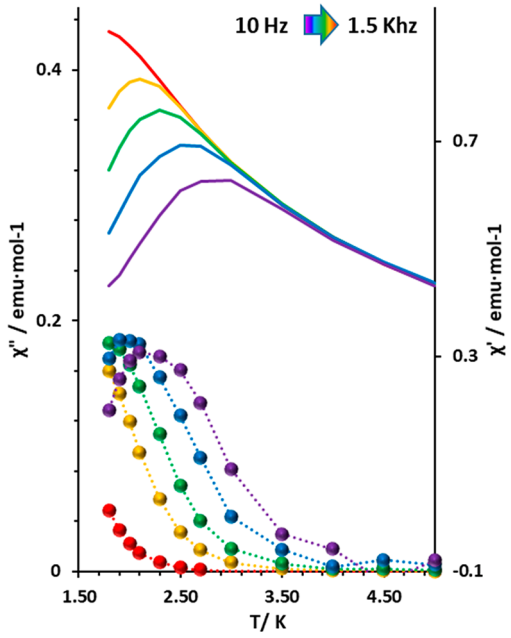

Figure 6. Temperature dependence of the AC signal in **1**.

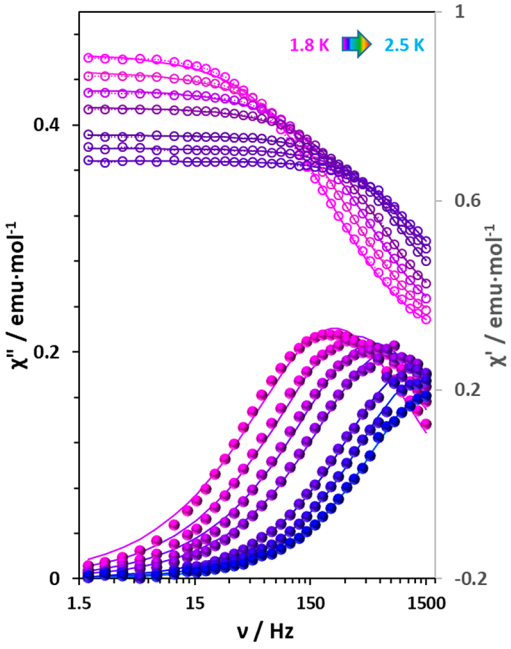

Figure 7. Frequency dependence of the AC signal in **1**.

been reported to exhibit SMM behavior, only one example[41] besides complex **1** contains a radical ligand. In that case, the relaxation time was not reported due to the lack of a clear maximum in the out-of-phase AC susceptibility.

3.4. Computational Studies. Density functional theory calculations were performed on **1** to evaluate its electronic structure in greater detail. Using the molecular structure derived from crystallographically determined coordinates, initial single-point energies that used the BP86 functional revealed that the quartet state was lower in energy than the sextet, which is consistent with the experimental finding. Consequently, the quartet wave function was used for the optimization. DFT (BP86) predicts a tetrahedral geometric structure, which is in close agreement with the structure derived from the X-ray crystallography of **1**. Specifically, two of the thioether arms are coordinated to the iron at Fe−S distances of 2.285 and 2.288 Å, with an S−Fe−S angle of 94.4° (experimental Fe−S 2.316(1) and 2.334(1) Å and a S−Fe−S angle of 93.84(2)°). The computed Fe−N distances of 1.981 and 1.989 Å and the N−Fe−N angle of 85.4° compare well to the experimentally determined metric parameters (Fe−N 1.971(2) and 1.976(2) Å and a N−Fe−N angle of 84.92(6)°). The ligand bond lengths of C−N 1.349 and 1.347 Å and C−C 1.408 Å are consistent with the formulation of L as a monoanionic π-radical (experimental C−N 1.336(2) and 1.332(2) Å and C−C 1.395(3)).

The inspection of the frontier molecular orbitals from a single-point calculation (TPSSh) of **1** further supports a high-spin ferrous and L π-radical assignment (Figure 8). Using the

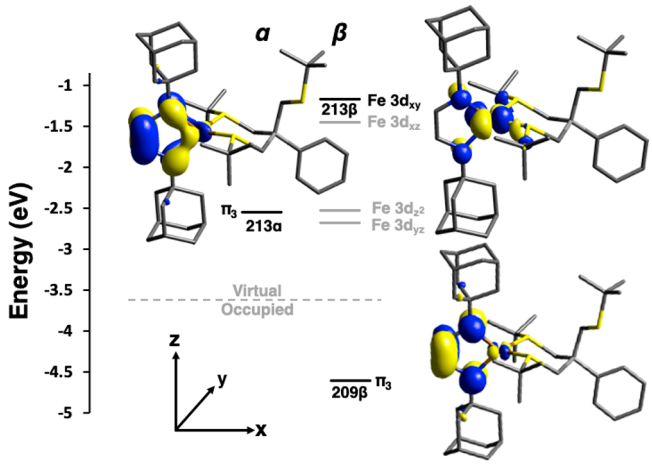

Figure 8. Quantitative FMO diagram of **1** (TPSSh/Fe,S,N:Def2-TZVP;C,H,B:Def2-SVP).

unfilled orbitals, which reflect the uncompensated spin of their filled counterparts, four spin-down, predominantly iron, 3d orbitals were found, which is reflective of a high-spin ferrous (d^6) electronic structure. A spin-up π^* orbital of the α-diimine ligand was also identified (213α), indicating the presence of an α-diimine radical ligand. The $\langle S^2\rangle$ value of this quartet was 4.45 and became 3.77 after the removal of the first spin contaminant, which is close to the expected value of 3.75 for an $S = 3/2$ system. Thus, J can be estimated using the formalism of Yamaguchi by

$$J = \frac{^{LS}E - {}^{HS}E}{^{LS}\langle S^2\rangle - {}^{HS}\langle S^2\rangle} \quad (3)$$

where ^{LS}E and ^{HS}E are the SCF energies of the $S = 3/2$ and $S = 5/2$ states, respectively, and $\langle S^2\rangle$ is the spin expectation value of the respective calculation. This yielded a sizable J value of -657 cm^{-1}. When interpreted in the context of the molecular orbitals, there exists a single *efficient* pathway for magnetic exchange out of four possible pathways for this antiferromagnetic coupling, wherein the ligand radical strongly interacts with the Fe 3d$_{xy}$ (213β) orbital to strongly stabilize the $S = 3/2$ state.

TD-DFT (TPSSh) calculations were performed to aid in the assignment of the electronic excited states. For computational efficiency, a truncated model of **1** was created (**1***) where the heavy-atom positions were frozen to the larger model positions (see the Computational Methods section). This choice was

https://doi.org/10.1021/acs.inorgchem.1c00214
Inorg. Chem. 2021, 60, 6480−6491

justified based on the nearly identical quartet−sextet splitting and *g*-tensor calculations (see below). Vacuum and solvated calculations were performed on **1*** and both yielded qualitatively similar results compared to those of the experimental spectrum, lending confidence to the band assignments (Figure S6 and Table S7) and the overall electronic structure model. The prominent feature at 402 nm in the experimental spectrum was determined to be two closely spaced transitions at 402 and 404 nm, which are composed of coordinated thioether S $p_\sigma \rightarrow$ Fe $3d_{yz}$ and thioether S $p_\sigma \rightarrow$ L π_3 transitions in nature. The shoulder on the low-energy side of this transition, which was experimentally observed at 456 nm, is correlated to a TD-DFT transition at 496 nm, L $\pi_3 \rightarrow$ Fe d_{xy}. The dominant higher-energy transition was predicted to be L $\pi \rightarrow$ L π^* overlapped with less-intense thioether S $p_\sigma \rightarrow$ Fe d transitions.

The close spacing of the LMCT transitions and the significant spin contamination in the quartet from the sextet led us to consider the electron correlation with a benchmark CCSD(T) methodology and the multireference character with a CAS methodology. These calculations used the truncated model **1*** for computational feasibility. CCSD(T) incorrectly orders the sextet state as lower in energy than the quartet. Moreover, the calculation of the fractional occupation number-weighted electron density (Table S10) demonstrated significant Fermi smearing ($\rho^{FOD} = 1.68$) across the Fe and diimine radical−ligand π-system. The large delocalized ρ^{FOD} value indicates a true multireference wave function and suggests that a multiconfigurational methodology (i.e., CAS) should be employed at minimum.

The broken-symmetry DFT wave function of **1*** was used to generate quasi-restricted orbitals (QROs) for the initial CASSCF guess. The active space was systematically expanded by the addition of occupied and virtual orbitals to include orbitals with occupancy *N* between 0.005 and 1.995. Guided by the plot of the FOD, the π-system of the alpha-diimine, S p_σ orbitals, and the Fe 3d set were considered, but the final 11 electrons in the 14 orbitals solution also included the "double-shell" unoccupied Fe 4d orbitals[99] and not the S p_σ orbitals. This calculation yielded a strongly multiconfigurational ground state spanning the following three configurations (Table S11): 48% $(3d_{xy})^2(\pi_3)^0$, 29% $(3d_{xy})^1(\pi_3)^1$, and 18% $(3d_{xy})^0(\pi_3)^2$ (invariant active orbitals were omitted). The $(3d_{xy})^1(\pi_3)^1$ configuration is equivalent to the broken-symmetry Kohn−Sham determinant. These three configurations mirror the common resonance forms of the α-diimine ligand and suggest a significant ionic contribution to bonding, which is weighted toward the Fe(I) and neutral α-diimine description ($-5J$ = 1706 [1992] cm^{-1} (square brackets indicate the NEVPT2 corrected value)). An investigation of quartet and sextet excited states of the final CAS(11,14) wave function revealed several low-lying states on each spin manifold. Thus, final molecular orbitals were optimized by the systematic inclusion of quartet and sextet roots; ultimately, five of each spin were equally weighted to generate a state-averaged (SA) CAS solution. The SA-CAS ground state configurations indicate a less ionic ground state, and inclusion of the four low-lying quartet excited states shift the configurational weighting toward the Fe(II)−α-diimine radical description (Figure 9 and Table S13). The first sextet excited state is composed of a single dominant configuration, $(3d_{xy})^1(\pi_3)^1$, regardless of if the orbitals are state averaged, again reflecting that this state is well-described by a single determinant. The state-averaged

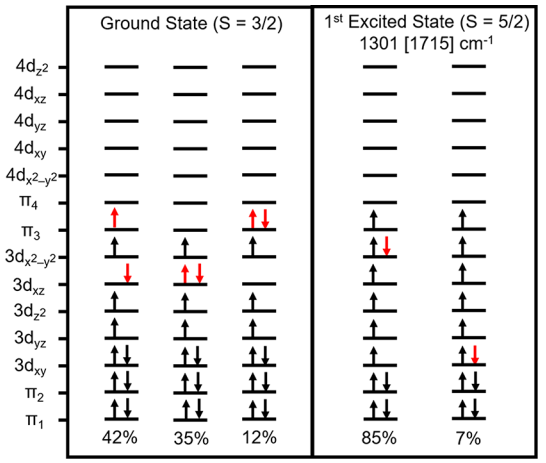

Figure 9. Dominant configurations in the ground state ($S = 3/2$) and first excited state ($S = 5/2$) based on a CAS(11,14) calculation using state-averaged orbitals (5 quartet roots +5 sextet roots). The energy in the square brackets is the NEVPT2 corrected.

quartet−sextet energy gap ($-5J$) is 1301 [1715] cm^{-1} (the NEVPT2 is indicated by square brackets), which is indicative of the strong antiferromagnetic coupling.

With the above computational methods, we further investigated the spectroscopic properties using the truncated model **1*** to compare them with the experimental values (Tables 1 and S14). Mössbauer parameters for the quadrupole splitting ΔE_Q (−2.995 mm/s) and the isomer shift δ (0.523 mm/s) were computed by DFT(TPSSh) and match reasonably well with the experimental values (δ 0.60 mm/s and ΔE_Q = −4.03 mm/s), further indicating that the DFT model effectively describes the electronic structure of **1**. The calculation of the isomer shift requires fitting constants that are not available for CAS or CCSD(T). Nonetheless, the quadrupole splitting values can be directly calculated with these methods (CAS ΔE_Q = −3.572 mm/s CCSD(T) ΔE_Q = −3.560 mm/s) and are in good agreement with the experimental value. Computational EPR parameters (g_{11}, g_{22}, g_{33}, D, and E/D) were also computed. The computational values were in agreement with the experimental values, with all methods yielding negative D values; however, the CAS approaches overestimate the rhombicity, leading to E/D ratios significantly larger than the experimental values.

CONCLUSIONS

The idea of incorporating a radical ligand in the design of SMMs has received increasing attention in recent years. In this context, we described the first α-diiminato radical-containing mononuclear transition metal SMM, namely, [κ^2-PhTt^{tBu}]Fe-(AdNCHCHNAd) (**1**), and its analogue [κ^2-PhTt^{tBu}]Fe-(CyNCHCHNCy) (**2**). X-ray crystallography; electronic, EPR and Mössbauer spectroscopies; SQUID magnetometry; and DFT and CAS calculations were employed to fully elucidate the geometric and electronic structures. **1** and **2** feature nearly identical geometric and electronic structures, both of which contain pseudotetrahedral high-spin iron(II) ions antiferromagnetically coupled to the α-diiminato radicals. The variable-temperature magnetic susceptibility data of **1** suggest strong exchange coupling between the high-spin ferrous ion and the ligand radical, with an estimated coupling constant $J < -250$ cm^{-1}. Such a strong magnetic coupling is supported by theoretical calculations. In particular, exper-

https://doi.org/10.1021/acs.inorgchem.1c00214
Inorg. Chem. 2021, 60, 6480−6491

Table 1. Comparison of Computationally Derived Spectral Parameters with Experiment[a]

	DFT	CCSD(T)[b]	CAS(11,14)[c]	SA-CAS(11,14)[d]	EXP
			magnetic coupling		
J (cm^{-1})	−657	+284	−341 [−398]	−260 [−343]	<−250
			Mössbauer		
δ (mm/s)[e]	0.523				0.60
ΔE_Q (mm/s)	−2.995	−3.560	−3.572	−3.571	−4.03
			electron paramagnetic resonance		
$g11$	2.015	2.020	2.018 [2.023]	2.039 [2.035]	1.84
g22	2.032	2.052	2.042 [2.045]	2.063 [2.058]	1.94
$g33$	2.034	2.103	2.073 [2.081]	2.101 [2.092]	2.19
D (cm^{-1})[f]	−3.554	−1.324	−2.368 [−2.550]	−2.671 [−2.526]	−2.65
E/D[f]	0.086	0.043	0.321 [0.279]	0.277 [0.291]	0.073

[a]Values in square brackets are SC-NEVPT2 corrected values. [b]CCSD(T) with the domain local-pair natural orbital approximation. [c]Used the ground-state orbitals with five quartet roots and five sextet roots. [d]Used state-averaged orbitals with five quartet roots and five sextet roots. [e]CCSD and CAS calibration tables for the calculation of δ are not available; [f]Zero-field splitting parameters from the second-order spin−orbit coupling contribution.

imentally gauged DFT calculations predict an exceptionally large coupling constant of $J = -657$ cm^{-1}.

EPR spectroscopy, SQUID magnetometry, and computational analysis suggest that **1** possesses an easy-axis anisotropy, with axial ZFS -4 $cm^{-1} < D < -1$ cm^{-1}. Consistent with a negative D value and a large $|J|$ value, which likely suppress quantum tunneling processes, **1** exhibits slow magnetic relaxation behavior with an energy barrier close to the theoretical maximum $2|D|$. These results demonstrate that incorporating a strongly coupled radical ligand, such as the α-diiminato radical, into mononuclear transition metal complexes can be an effective route to SMMs.

Further insight into the electronic structure of **1** and **2** was provided by calibrated CAS calculations, which revealed that the ground state Fe(II)−α-diiminato radical configuration has significant ionic contributions that are weighted specifically toward the Fe(I)-neutral α-diimine formalism. While it is unknown how the dynamics of the magnetic relaxation correlate with the electronic structure, it will be of interest to interrogate the structure−property relationship in the future by switching to more electron-accepting α-diimine ligands so that the Fe(II)−α-diiminato radical state is more dominant. Preparing new Fe(II)−α-diiminato radical complexes with larger $|D|$ values and thus higher energy barriers to magnetic relaxation is also of interest.

■ ASSOCIATED CONTENT

Supporting Information

The Supporting Information is available free of charge at https://pubs.acs.org/doi/10.1021/acs.inorgchem.1c00214.

Computational and EPR simulation details, crystallographic data, additional magnetic and Mössbauer data, and additional computational results (PDF)

Accession Codes

CCDC 1974684−1974685 contain the supplementary crystallographic data for this paper. These data can be obtained free of charge via www.ccdc.cam.ac.uk/data_request/cif, or by emailing data_request@ccdc.cam.ac.uk, or by contacting The Cambridge Crystallographic Data Centre, 12 Union Road, Cambridge CB2 1EZ, UK; fax: +44 1223 336033.

■ AUTHOR INFORMATION

Corresponding Authors

Charles G. Riordan − *Department of Chemistry & Biochemistry, University of Delaware, Newark, Delaware 19716, United States;* orcid.org/0000-0002-8572-4571; Email: riordan@udel.edu

Kim R. Dunbar − *Department of Chemistry, Texas A&M University, College Station, Texas 77842-3012, United States;* orcid.org/0000-0001-5728-7805; Email: dunbar@chem.tamu.edu

Matthew T. Kieber-Emmons − *Department of Chemistry, University of Utah, Salt Lake City, Utah 84112-0850, United States;* orcid.org/0000-0002-6357-5579; Email: matthew.kieber-emmons@utah.edu

Authors

Peng Wang − *Department of Chemistry & Biochemistry, University of Delaware, Newark, Delaware 19716, United States;* orcid.org/0000-0002-7991-2541

Mohamed R. Saber − *Department of Chemistry, Texas A&M University, College Station, Texas 77842-3012, United States; Department of Chemistry, Fayoum University, Fayoum 63514, Egypt*

Peter E. VanNatta − *Department of Chemistry, University of Utah, Salt Lake City, Utah 84112-0850, United States;* orcid.org/0000-0003-1360-579X

Glenn P. A. Yap − *Department of Chemistry & Biochemistry, University of Delaware, Newark, Delaware 19716, United States*

Codrina V. Popescu − *Department of Chemistry, University of Saint Thomas, Saint Paul, Minnesota 55105, United States;* orcid.org/0000-0003-2369-3383

Christopher C. Scarborough − *Department of Chemistry, Emory University, Atlanta, Georgia 30322, United States; Syngenta Crop Protection AG, CH-4332 Stein, Switzerland*

Complete contact information is available at: https://pubs.acs.org/10.1021/acs.inorgchem.1c00214

Notes

The authors declare no competing financial interest.

■ ACKNOWLEDGMENTS

C.G.R. acknowledges the financial support of the National Science Foundation (NSF) through Award CHE-1112035.

M.K.E. acknowledges the financial support of the Department of Energy (DOE) through Award DE-SC0020954. K.R.D. gratefully thanks the National Science Foundation (NSF CHE-1808779) and the Welch Foundation (A-1449) for financial support. We thank Professor Michael Green and Ms. Elizabeth Onderko, UC-Irvine, for collecting the EPR spectral data.

REFERENCES

(1) Kaim, W. Manifestations of Noninnocent Ligand Behavior. *Inorg. Chem.* **2011**, *50* (20), 9752−9765.
(2) Kaim, W.; Schwederski, B. Non-Innocent Ligands in Bioinorganic Chemistry—An Overview. *Coord. Chem. Rev.* **2010**, *254* (13), 1580−1588.
(3) Kaim, W. Chelate Rings of Different Sizes with Non-Innocent Ligands. *Dalton Trans.* **2019**, *48* (24), 8521−8529.
(4) Mondal, B.; Ye, S. Hidden Ligand Noninnocence: A Combined Spectroscopic and Computational Perspective. *Coord. Chem. Rev.* **2020**, *405*, 213115.
(5) Khan, F. F.; Chowdhury, A. D.; Lahiri, G. K. Bond Activations Assisted by Redox Active Ligand Scaffolds. *Eur. J. Inorg. Chem.* **2020**, *2020* (13), 1138−1146.
(6) Singh, B.; Indra, A. Role of Redox Active and Redox Non-Innocent Ligands in Water Splitting. *Inorg. Chim. Acta* **2020**, *506*, 119440.
(7) Broere, D.; Plessius, R.; van der Vlugt, J. I. New Avenues for Ligand-Mediated Processes - Expanding Metal Reactivity by the Use of Redox-Active Catechol, o-Aminophenol and o-Phenylenediamine Ligands. *Chem. Soc. Rev.* **2015**, *44*, 6886−6915.
(8) Lyaskovskyy, V.; de Bruin, B. Redox Non-Innocent Ligands: Versatile New Tools to Control Catalytic Reactions. *ACS Catal.* **2012**, *2* (2), 270−279.
(9) Luca, O. R.; Crabtree, R. H. Redox-Active Ligands in Catalysis. *Chem. Soc. Rev.* **2013**, *42* (4), 1440−1459.
(10) Rajput, A.; Sharma, A. K.; Barman, S. K.; Saha, A.; Mukherjee, R. Valence Tautomerism and Delocalization in Transition Metal Complexes of O-Amidophenolates and Other Redox-Active Ligands. Some Recent Results. *Coord. Chem. Rev.* **2020**, *414*, 213240.
(11) Tezgerevska, T.; Alley, K. G.; Boskovic, C. Valence Tautomerism in Metal Complexes: Stimulated and Reversible Intramolecular Electron Transfer between Metal Centers and Organic Ligands. *Coord. Chem. Rev.* **2014**, *268*, 23−40.
(12) Demir, S.; Jeon, I.-R.; Long, J. R.; Harris, T. D. Radical Ligand-Containing Single-Molecule Magnets. *Coord. Chem. Rev.* **2015**, *289*−*290*, 149−176.
(13) Graf, M.; Wolmershäuser, G.; Kelm, H.; Demeschko, S.; Meyer, F.; Krüger, H.-J. Temperature-Induced Spin-Transition in a Low-Spin Cobalt(II) Semiquinonate Complex. *Angew. Chem., Int. Ed.* **2010**, *49* (5), 950−953.
(14) Schmitz, M.; Seibel, M.; Kelm, H.; Demeshko, S.; Meyer, F.; Krüger, H.-J. How Does a Coordinated Radical Ligand Affect the Spin Crossover Properties in an Octahedral Iron(II) Complex? *Angew. Chem., Int. Ed.* **2014**, *53* (23), 5988−5992.
(15) Khusniyarov, M. M.; Weyhermüller, T.; Bill, E.; Wieghardt, K. Reversible Electron Transfer Coupled to Spin Crossover in an Iron Coordination Salt in the Solid State. *Angew. Chem., Int. Ed.* **2008**, *47* (7), 1228−1231.
(16) Khusniyarov, M. M.; Bill, E.; Weyhermüller, T.; Bothe, E.; Harms, K.; Sundermeyer, J.; Wieghardt, K. Characterization of Three Members of the Electron-Transfer Series [Fe(pda)2]n (n = 2-, 1-, 0) by Spectroscopy and Density Functional Theoretical Calculations [pda = Redox Non-innocent Derivatives of N,N′-Bis-(pentafluorophenyl)-o-phenylenediamide(2-, 1.-, 0)]. *Chem. - Eur. J.* **2008**, *14* (25), 7608−7622.
(17) Wang, P.; Yap, G. P. A.; Riordan, C. G. Five-Coordinate MII-Semiquinonate (M = Fe, Mn, Co) Complexes: Reactivity Models of the Catechol Dioxygenases. *Chem. Commun.* **2014**, *50* (44), 5871−5873.
(18) Wang, P.; Killian, M. M.; Saber, M. R.; Qiu, T.; Yap, G. P. A.; Popescu, C. V.; Rosenthal, J.; Dunbar, K. R.; Brunold, T. C.; Riordan, C. G. Electronic, Magnetic, and Redox Properties and O2 Reactivity of Iron(II) and Nickel(II) o-Semiquinonate Complexes of a Tris(Thioether) Ligand: Uncovering the Intradiol Cleaving Reactivity of an Iron(II) o-Semiquinonate Complex. *Inorg. Chem.* **2017**, *56* (17), 10481−10495.
(19) Wang, P.; Yap, G. P. A.; Riordan, C. G. Synthesis, Characterization and O_2 Reactivity of a Bioinspired Cobalt(II)-Catecholate Complex. *Inorg. Chim. Acta* **2019**, *488*, 49−55.
(20) Wang, P. *Tris(Thioether)-Supported Base Metal Complexes with Redox-Active Dioxolene and α-Diimine Ligands*. Ph.D. Thesis, University of Delaware, Newark, DE, 2015. https://udspace.udel.edu/handle/19716/17686. This paper is adapted, in part, from the thesis.
(21) Efthymiou, C.; Winterlich, M.; Papatriantafyllopoulou, C. Breakthrough in Radical-Bridged Single-Molecule Magnets. In *Single-Molecule Magnets: Molecular Architectures and Building Blocks for Spintronics*; Wiley-VCH, Weinheim, Germany, 2018; pp 315−351..
(22) Jeon, I.-R.; Park, J. G.; Xiao, D. J.; Harris, T. D. An Azophenine Radical-Bridged Fe2 Single-Molecule Magnet with Record Magnetic Exchange Coupling. *J. Am. Chem. Soc.* **2013**, *135* (45), 16845−16848.
(23) DeGayner, J. A.; Jeon, I.-R.; Harris, T. D. A Series of Tetraazalene Radical-Bridged M2 (M = CrIII, MnII, FeII, CoII) Complexes with Strong Magnetic Exchange Coupling. *Chem. Sci.* **2015**, *6* (11), 6639−6648.
(24) Thorarinsdottir, A. E.; Bjornsson, R.; Harris, T. D. Insensitivity of Magnetic Coupling to Ligand Substitution in a Series of Tetraoxolene Radical-Bridged Fe2 Complexes. *Inorg. Chem.* **2020**, *59* (7), 4634−4649.
(25) Chakarawet, K.; Harris, T. D.; Long, J. R. Semiquinone Radical-Bridged M2 (M = Fe, Co, Ni) Complexes with Strong Magnetic Exchange Giving Rise to Slow Magnetic Relaxation. *Chem. Sci.* **2020**, *11* (31), 8196−8203.
(26) Albold, U.; Bamberger, H.; Hallmen, P. P.; van Slageren, J.; Sarkar, B. Strong Exchange Couplings Drastically Slow Down Magnetization Relaxation in an Air-Stable Cobalt(II)-Radical Single-Molecule Magnet (SMM). *Angew. Chem., Int. Ed.* **2019**, *58* (29), 9802−9806.
(27) Ma, X.; Suturina, E. A.; De, S.; Négrier, P.; Rouzières, M.; Clérac, R.; Dechambenoit, P. A Redox-Active Bridging Ligand to Promote Spin Delocalization, High-Spin Complexes, and Magnetic Multi-Switchability. *Angew. Chem., Int. Ed.* **2018**, *57* (26), 7841−7845.
(28) Wang, Y.; Li, J.; Zhang, L.; Chen, C.; Feng, R.; Zhao, Y.; Zhang, Y.-Q.; Tan, G.; Song, Y.; Wang, X. Magnetic on-off Switching in Redox Non-Innocent Ligand Bridged Binuclear Cobalt Complexes. *Dalton Trans.* **2018**, *47* (48), 17211−17215.
(29) Woods, T. J.; Ballesteros-Rivas, M. F.; Ostrovsky, S. M.; Palii, A. V.; Reu, O. S.; Klokishner, S. I.; Dunbar, K. R. Strong Direct Magnetic Coupling in a Dinuclear CoII Tetrazine Radical Single-Molecule Magnet. *Chem. - Eur. J.* **2015**, *21* (29), 10302−10305.
(30) Fortier, S.; Le Roy, J. J.; Chen, C.-H.; Vieru, V.; Murugesu, M.; Chibotaru, L. F.; Mindiola, D. J.; Caulton, K. G. A Dinuclear Cobalt Complex Featuring Unprecedented Anodic and Cathodic Redox Switches for Single-Molecule Magnet Activity. *J. Am. Chem. Soc.* **2013**, *135* (39), 14670−14678.
(31) Craig, G. A.; Murrie, M. 3d Single-Ion Magnets. *Chem. Soc. Rev.* **2015**, *44* (8), 2135−2147.
(32) Frost, J. M.; Harriman, K. L. M.; Murugesu, M. The Rise of 3-d Single-Ion Magnets in Molecular Magnetism: Towards Materials from Molecules? *Chem. Sci.* **2016**, *7* (4), 2470−2491.
(33) Gass, I. A.; Tewary, S.; Nafady, A.; Chilton, N. F.; Gartshore, C. J.; Asadi, M.; Lupton, D. W.; Moubaraki, B.; Bond, A. M.; Boas, J. F.; Guo, S.-X.; Rajaraman, G.; Murray, K. S. Observation of Ferromagnetic Exchange, Spin Crossover, Reductively Induced Oxidation, and Field-Induced Slow Magnetic Relaxation in Monomeric Cobalt Nitroxides. *Inorg. Chem.* **2013**, *52* (13), 7557−7572.

https://doi.org/10.1021/acs.inorgchem.1c00214
Inorg. Chem. 2021, 60, 6480−6491

(34) Kanegawa, S.; Karasawa, S.; Nakano, M.; Koga, N. Magnetic Behavior of Tetrakis[4-(N-Tert-Butyl-N-Oxylamino)Pyridine]Bis-(Isocyanato-N)Cobalt(II) in Frozen Solution. *Chem. Commun.* **2004**, No. 15, 1750−1751.
(35) Kanegawa, S.; Karasawa, S.; Maeyama, M.; Nakano, M.; Koga, N. Crystal Design of Monometallic Single-Molecule Magnets Consisting of Cobalt-Aminoxyl Heterospins. *J. Am. Chem. Soc.* **2008**, *130* (10), 3079−3094.
(36) Karasawa, S.; Nakano, K.; Yoshihara, D.; Yamamoto, N.; Tanokashira, J.; Yoshizaki, T.; Inagaki, Y.; Koga, N. Magnetic Properties of 1:2 Mixed Cobalt(II) Salicylaldehyde Schiff-Base Complexes with Pyridine Ligands Carrying High-Spin Carbenes (Scar = 2/2, 4/2, 6/2, and 8/2) in Dilute Frozen Solutions: Role of Organic Spin in Heterospin Single-Molecule Magnets. *Inorg. Chem.* **2014**, *53* (11), 5447−5457.
(37) Karasawa, S.; Koga, N. Magnetic Properties after Irradiation of 1:4 Complexes Consisting of CoX2, X = NCS-, Cl-, and NCO-, and Phenylpyridyldiazomethane in Dilute Frozen Solutions: Axial Ligand Effect in Heterospin Single-Molecule Magnets. *Inorg. Chem.* **2011**, *50* (11), 5186−5195.
(38) Karasawa, S.; Nakano, K.; Tanokashira, J.; Yamamoto, N.; Yoshizaki, T.; Koga, N. Magnetic Properties of 1:4 Complexes of CoCl2 and Pyridines Carrying Carbenes (S0 = 4/2, 6/2, and 8/2) in Diluted Frozen Solution; Influence of Carbene Multiplicity on Heterospin Single-Molecule Magnets. *Dalton Trans.* **2012**, *41* (44), 13656−13667.
(39) Yoshihara, D.; Karasawa, S.; Koga, N. Cyclic Single-Molecule Magnet in Heterospin System. *J. Am. Chem. Soc.* **2008**, *130* (32), 10460−10461.
(40) Yoshihara, D.; Karasawa, S.; Koga, N. Heterospin Single-Molecule Magnets with Extra-Large Anisotropic Barrier. *Polyhedron* **2011**, *30* (18), 3211−3217.
(41) Michalowicz, C. A.; Mills, M. B.; Song, E.; Soldatov, D. V.; Boyle, P. D.; Rouzières, M.; Clérac, R.; Preuss, K. E. Slow Magnetization Dynamics in a Six-Coordinate Fe(II)-Radical Complex. *Dalton Trans.* **2019**, *48* (14), 4514−4519.
(42) Bai, Y.; Chen, W.; Li, J.; Cui, C. Chemistry of S-, p- and f-Block Metal Complexes with Ene-Diamido Ligands. *Coord. Chem. Rev.* **2019**, *383*, 132−154.
(43) Nikolaevskaya, E. N.; Druzhkov, N. O.; Syroeshkin, M. A.; Egorov, M. P. Chemistry of Diazadiene Type Ligands with Extra Coordination Groups. Prospects of Reactivity. *Coord. Chem. Rev.* **2020**, *417*, 213353.
(44) Wang, F.; Chen, C. A Continuing Legend: The Brookhart-Type α-Diimine Nickel and Palladium Catalysts. *Polym. Chem.* **2019**, *10* (19), 2354−2369.
(45) Muresan, N.; Lu, C. C.; Ghosh, M.; Peters, J. C.; Abe, M.; Henling, L. M.; Weyhermöller, T.; Bill, E.; Wieghardt, K. Bis(α-Diimine)Iron Complexes: Electronic Structure Determination by Spectroscopy and Broken Symmetry Density Functional Theoretical Calculations. *Inorg. Chem.* **2008**, *47* (11), 4579−4590.
(46) Muresan, N.; Chlopek, K.; Weyhermüller, T.; Neese, F.; Wieghardt, K. Bis(α-Diimine)Nickel Complexes: Molecular and Electronic Structure of Three Members of the Electron-Transfer Series [Ni(L)2]z (z = 0, 1+, 2+) (L = 2-Phenyl-1,4-Bis(Isopropyl)-1,4-Diazabutadiene). A Combined Experimental and Theoretical Study. *Inorg. Chem.* **2007**, *46* (13), 5327−5337.
(47) Ghosh, M.; Sproules, S.; Weyhermüller, T.; Wieghardt, K. (α-Diimine)Chromium Complexes: Molecular and Electronic Structures; A Combined Experimental and Density Functional Theoretical Study. *Inorg. Chem.* **2008**, *47* (13), 5963−5970.
(48) Khusniyarov, M. M.; Weyhermüller, T.; Bill, E.; Wieghardt, K. Tuning the Oxidation Level, the Spin State, and the Degree of Electron Delocalization in Homo- and Heteroleptic Bis(α-Diimine) Iron Complexes. *J. Am. Chem. Soc.* **2009**, *131* (3), 1208−1221.
(49) Das, C.; Upadhyay, A.; Shanmugam, M. Influence of Radicals on Magnetization Relaxation Dynamics of Pseudo-Octahedral Lanthanide Iminopyridyl Complexes. *Inorg. Chem.* **2018**, *57* (15), 9002−9011.
(50) Long, J.; Skvortsov, G. G.; Cherkasov, A. V.; Lyssenko, K. A.; Poddel'sky, A. I.; Guari, Y.; Larionova, J.; Trifonov, A. A. Synthesis, Structure and Magnetic Properties of a Series of Ln(III) Complexes with Radical-Anionic Iminopyridine Ligands: Effect of Lanthanide Ions on the Slow Relaxation of the Magnetization. *Dalton Trans.* **2019**, *48* (32), 12018−12022.
(51) Long, J.; Tolpygin, A. O.; Cherkasov, A. V.; Lyssenko, K. A.; Guari, Y.; Larionova, J.; Trifonov, A. A. Single-Molecule Magnet Behavior in Heterolopetic Dy3+-Chloro-Diazabutadiene Complexes: Influence of the Nuclearity and Ligand Redox State. *Dalton Trans.* **2020**, *49* (34), 11890−11901.
(52) Yan, H.; Wu, B.; Meng, Y.-S.; Zhang, W.-X.; Xi, Z. Synthesis, Structure, and Magnetic Properties of Rare-Earth Bis-(Diazabutadiene) Diradical Complexes. *Inorg. Chem.* **2021**, *60* (3), 1315−1319.
(53) Mock, M. T.; Popescu, C. V.; Yap, G. P. A.; Dougherty, W. G.; Riordan, C. G. Monovalent Iron in a Sulfur-Rich Environment. *Inorg. Chem.* **2008**, *47* (6), 1889−1891.
(54) Kliegman, J. M.; Barnes, R. K. Glyoxal Derivatives—I: Conjugated Aliphatic Diimines from Glyoxal and Aliphatic Primary Amines. *Tetrahedron* **1970**, *26* (10), 2555−2560.
(55) Linden, H. B. Liquid Injection Field Desorption Ionization: A New Tool for Soft Ionization of Samples Including Air-Sensitive Catalysts and Non-Polar Hydrocarbons. *Eur. J. Mass Spectrom.* **2004**, *10* (4), 459−468.
(56) Gross, J. H.; Nieth, N.; Linden, H. B.; Blumbach, U.; Richter, F. J.; Tauchert, M. E.; Tompers, R.; Hofmann, P. Liquid Injection Field Desorption/Ionization of Reactive Transition Metal Complexes. *Anal. Bioanal. Chem.* **2006**, *386* (1), 52−58.
(57) Evans, D. F. The Determination of the Paramagnetic Susceptibility of Substances in Solution by Nuclear Magnetic Resonance. *J. Chem. Soc.* **1959**, No. 0, 2003−2005.
(58) Live, D. H.; Chan, S. I. Bulk susceptibility corrections in nuclear magnetic resonance experiments using superconducting solenoids. *Anal. Chem.* **1970**, *42* (7), 791−792.
(59) Bain, G. A.; Berry, J. F. Diamagnetic Corrections and Pascal's Constants. *J. Chem. Educ.* **2008**, *85* (4), 532.
(60) Stoll, S.; Schweiger, A. EasySpin, a Comprehensive Software Package for Spectral Simulation and Analysis in EPR. *J. Magn. Reson.* **2006**, *178* (1), 42−55.
(61) Frisch, M. J.; Trucks, G. W.; Schlegel, H. B.; Scuseria, G. E.; Robb, M. A.; Cheeseman, J. R.; Scalmani, G.; Barone, V.; Petersson, G. A.; Nakatsuji, H.; Li, X.; Caricato, M.; Marenich, A. V.; Bloino, J.; Janesko, B. G.; Gomperts, R.; Mennucci, B.; Hratchian, H. P.; Ortiz, J. V.; Izmaylov, A. F.; Sonnenberg, J. L.; Williams-Young, D.; Ding, F.; Lipparini, F.; Egidi, F.; Goings, J.; Peng, B.; Petrone, A.; Henderson, T.; Ranasinghe, D.; Zakrzewski, V. G.; Gao, J.; Rega, N.; Zheng, G.; Liang, W.; Hada, M.; Ehara, M.; Toyota, K.; Fukuda, R.; Hasegawa, J.; Ishida, M.; Nakajima, T.; Honda, Y.; Kitao, O.; Nakai, H.; Vreven, T.; Throssell, K.; Montgomery, J. A., Jr.; Peralta, J. E.; Ogliaro, F.; Bearpark, M. J.; Heyd, J. J.; Brothers, E. N.; Kudin, K. N.; Staroverov, V. N.; Keith, T. A.; Kobayashi, R.; Normand, J.; Raghavachari, K.; Rendell, A. P.; Burant, J. C.; Iyengar, S. S.; Tomasi, J.; Cossi, M.; Millam, J. M.; Klene, M.; Adamo, C.; Cammi, R.; Ochterski, J. W.; Martin, R. L.; Morokuma, K.; Farkas, O.; Foresman, J. B.; Fox, D. J. *Gaussian 16*, rev. C.01; Gaussian, Inc.: Wallingford, CT, 2016.
(62) Becke, A. D. Density-Functional Exchange-Energy Approximation with Correct Asymptotic Behavior. *Phys. Rev. A: At., Mol., Opt. Phys.* **1988**, *38* (6), 3098−3100.
(63) Perdew, J. P. Density-Functional Approximation for the Correlation Energy of the Inhomogeneous Electron Gas. *Phys. Rev. B: Condens. Matter Mater. Phys.* **1986**, *33* (12), 8822−8824.
(64) Weigend, F.; Ahlrichs, R. Balanced Basis Sets of Split Valence, Triple Zeta Valence and Quadruple Zeta Valence Quality for H to Rn: Design and Assessment of Accuracy. *Phys. Chem. Chem. Phys.* **2005**, *7* (18), 3297−3305.
(65) Kieber-Emmons, M. T. *Lumo*, ver. 1.3; Self-Published: Salt Lake City, UT, 2013.

https://doi.org/10.1021/acs.inorgchem.1c00214
Inorg. Chem. 2021, 60, 6480−6491

(66) Neese, F. The ORCA Program System. *Wiley Interdiscip. Rev.: Comput. Mol. Sci.* **2012**, *2* (1), 73−78.
(67) Neese, F. Software Update: The ORCA Program System, Version 4.0. *Wiley Interdiscip. Rev.: Comput. Mol. Sci.* **2018**, *8* (1), No. e1327.
(68) Grimme, S.; Hansen, A. A Practicable Real-Space Measure and Visualization of Static Electron-Correlation Effects. *Angew. Chem., Int. Ed.* **2015**, *54* (42), 12308−12313.
(69) Römelt, M.; Ye, S.; Neese, F. Calibration of Modern Density Functional Theory Methods for the Prediction of 57Fe Mössbauer Isomer Shifts: Meta-GGA and Double-Hybrid Functionals. *Inorg. Chem.* **2009**, *48* (3), 784−785.
(70) Møller, C.; Plesset, M. S. Note on an Approximation Treatment for Many-Electron Systems. *Phys. Rev.* **1934**, *46* (7), 618−622.
(71) Raghavachari, K.; Trucks, G. W.; Pople, J. A.; Head-Gordon, M. A Fifth-Order Perturbation Comparison of Electron Correlation Theories. *Chem. Phys. Lett.* **1989**, *157* (6), 479−483.
(72) Guo, Y.; Riplinger, C.; Becker, U.; Liakos, D. G.; Minenkov, Y.; Cavallo, L.; Neese, F. Communication: An Improved Linear Scaling Perturbative Triples Correction for the Domain Based Local Pair-Natural Orbital Based Singles and Doubles Coupled Cluster Method [DLPNO-CCSD(T)]. *J. Chem. Phys.* **2018**, *148* (1), 011101.
(73) Weigend, F.; Häser, M.; Patzelt, H.; Ahlrichs, R. RI-MP2: Optimized Auxiliary Basis Sets and Demonstration of Efficiency. *Chem. Phys. Lett.* **1998**, *294* (1), 143−152.
(74) Chilkuri, V. G.; DeBeer, S.; Neese, F. Ligand Field Theory and Angular Overlap Model Based Analysis of the Electronic Structure of Homovalent Iron-Sulfur Dimers. *Inorg. Chem.* **2020**, *59* (2), 984−995.
(75) Angeli, C.; Cimiraglia, R.; Malrieu, J.-P. N-Electron Valence State Perturbation Theory: A Spinless Formulation and an Efficient Implementation of the Strongly Contracted and of the Partially Contracted Variants. *J. Chem. Phys.* **2002**, *117* (20), 9138−9153.
(76) Bart, S. C.; Hawrelak, E. J.; Schmisseur, A. K.; Lobkovsky, E.; Chirik, P. J. Synthesis, Reactivity, and Solid State Structures of Four-Coordinate Iron(II) and Manganese(II) Alkyl Complexes. *Organometallics* **2004**, *23* (2), 237−246.
(77) Albers, A.; Demeshko, S.; Dechert, S.; Bill, E.; Bothe, E.; Meyer, F. The Complete Characterization of a Reduced Biomimetic [2Fe-2S] Cluster. *Angew. Chem., Int. Ed.* **2011**, *50* (39), 9191−9194.
(78) Albers, A.; Demeshko, S.; Pröpper, K.; Dechert, S.; Bill, E.; Meyer, F. A Super-Reduced Diferrous [2Fe-2S] Cluster. *J. Am. Chem. Soc.* **2013**, *135* (5), 1704−1707.
(79) Chilton, N. F.; Anderson, R. P.; Turner, L. D.; Soncini, A.; Murray, K. S. PHI: A Powerful New Program for the Analysis of Anisotropic Monomeric and Exchange-Coupled Polynuclear d- and f-Block Complexes. *J. Comput. Chem.* **2013**, *34* (13), 1164−1175.
(80) Cowley, R. E.; Bill, E.; Neese, F.; Brennessel, W. W.; Holland, P. L. Iron(II) Complexes with Redox-Active Tetrazene (RNNNNR) Ligands. *Inorg. Chem.* **2009**, *48* (11), 4828−4836.
(81) Saber, M. R.; Dunbar, K. R. Ligands Effects on the Magnetic Anisotropy of Tetrahedral Cobalt Complexes. *Chem. Commun.* **2014**, *50* (82), 12266−12269.
(82) Vaidya, S.; Shukla, P.; Tripathi, S.; Rivière, E.; Mallah, T.; Rajaraman, G.; Shanmugam, M. Substituted versus Naked Thiourea Ligand Containing Pseudotetrahedral Cobalt(II) Complexes: A Comparative Study on Its Magnetization Relaxation Dynamics Phenomenon. *Inorg. Chem.* **2018**, *57* (6), 3371−3386.
(83) Cole, K. S.; Cole, R. H. Dispersion and Absorption in Dielectrics I. Alternating Current Characteristics. *J. Chem. Phys.* **1941**, *9* (4), 341−351.
(84) Zadrozny, J. M.; Xiao, D. J.; Atanasov, M.; Long, G. J.; Grandjean, F.; Neese, F.; Long, J. R. Magnetic Blocking in a Linear Iron(I) Complex. *Nat. Chem.* **2013**, *5* (7), 577−581.
(85) Samuel, P. P.; Mondal, K. C.; Amin Sk, N.; Roesky, H. W.; Carl, E.; Neufeld, R.; Stalke, D.; Demeshko, S.; Meyer, F.; Ungur, L.; Chibotaru, L. F.; Christian, J.; Ramachandran, V.; van Tol, J.; Dalal, N. S. Electronic Structure and Slow Magnetic Relaxation of Low-Coordinate Cyclic Alkyl(Amino) Carbene Stabilized Iron(I) Complexes. *J. Am. Chem. Soc.* **2014**, *136* (34), 11964−11971.
(86) Feng, X.; Mathonière, C.; Jeon, I.-R.; Rouzières, M.; Ozarowski, A.; Aubrey, M. L.; Gonzalez, M. I.; Clérac, R.; Long, J. R. Tristability in a Light-Actuated Single-Molecule Magnet. *J. Am. Chem. Soc.* **2013**, *135* (42), 15880−15884.
(87) Li, G.-L.; Wu, S.-Q.; Zhang, L.-F.; Wang, Z.; Ouyang, Z.-W.; Ni, Z.-H.; Su, S.-Q.; Yao, Z.-S.; Li, J.-Q.; Sato, O. Field-Induced Slow Magnetic Relaxation in an Octacoordinated Fe(II) Complex with Pseudo-D2d Symmetry: Magnetic, HF-EPR, and Theoretical Investigations. *Inorg. Chem.* **2017**, *56* (14), 8018−8025.
(88) Freedman, D. E.; Harman, W. H.; Harris, T. D.; Long, G. J.; Chang, C. J.; Long, J. R. Slow Magnetic Relaxation in a High-Spin Iron(II) Complex. *J. Am. Chem. Soc.* **2010**, *132* (4), 1224−1225.
(89) Harman, W. H.; Harris, T. D.; Freedman, D. E.; Fong, H.; Chang, A.; Rinehart, J. D.; Ozarowski, A.; Sougrati, M. T.; Grandjean, F.; Long, G. J.; Long, J. R.; Chang, C. J. Slow Magnetic Relaxation in a Family of Trigonal Pyramidal Iron(II) Pyrrolide Complexes. *J. Am. Chem. Soc.* **2010**, *132* (51), 18115−18126.
(90) Mathonière, C.; Lin, H.-J.; Siretanu, D.; Clérac, R.; Smith, J. M. Photoinduced Single-Molecule Magnet Properties in a Four-Coordinate Iron(II) Spin Crossover Complex. *J. Am. Chem. Soc.* **2013**, *135* (51), 19083−19086.
(91) Weismann, D.; Sun, Y.; Lan, Y.; Wolmershäuser, G.; Powell, A. K.; Sitzmann, H. High-Spin Cyclopentadienyl Complexes: A Single-Molecule Magnet Based on the Aryl-Iron(II) Cyclopentadienyl Type. *Chem. - Eur. J.* **2011**, *17* (17), 4700−4704.
(92) Werncke, C. G.; Bouammali, M.-A.; Baumard, J.; Suaud, N.; Martins, C.; Guihéry, N.; Vendier, L.; Zheng, J.; Sortais, J.-B.; Darcel, C.; Sabo-Etienne, S.; Sutter, J.-P.; Bontemps, S.; Pichon, C. Ising-Type Magnetic Anisotropy and Slow Relaxation of the Magnetization in Four-Coordinate Amido-Pyridine FeII Complexes. *Inorg. Chem.* **2016**, *55* (21), 10968−10977.
(93) Lin, P.-H.; Smythe, N. C.; Gorelsky, S. I.; Maguire, S.; Henson, N. J.; Korobkov, I.; Scott, B. L.; Gordon, J. C.; Baker, R. T.; Murugesu, M. Importance of Out-of-State Spin-Orbit Coupling for Slow Magnetic Relaxation in Mononuclear FeII Complexes. *J. Am. Chem. Soc.* **2011**, *133* (40), 15806−15809.
(94) Bodenstein, T.; Eichhöfer, A. Magnetic Anisotropy in Trigonal Planar Fe(II) Bis(Trimethylsilyl)Amido Complexes of the Type [Fe{N(SiMe3)2}2L]—Experiment and Theory. *Dalton Trans.* **2019**, *48* (41), 15699−15712.
(95) Zadrozny, J. M.; Atanasov, M.; Bryan, A. M.; Lin, C.-Y.; Rekken, B. D.; Power, P. P.; Neese, F.; Long, J. R. Slow Magnetization Dynamics in a Series of Two-Coordinate Iron(Ii) Complexes. *Chem. Sci.* **2013**, *4* (1), 125−138.
(96) Mossin, S.; Tran, B. L.; Adhikari, D.; Pink, M.; Heinemann, F. W.; Sutter, J.; Szilagyi, R. K.; Meyer, K.; Mindiola, D. J. A Mononuclear Fe(III) Single Molecule Magnet with a 3/2↔5/2 Spin Crossover. *J. Am. Chem. Soc.* **2012**, *134* (33), 13651−13661.
(97) Feng, X.; Hwang, S. J.; Liu, J.-L.; Chen, Y.-C.; Tong, M.-L.; Nocera, D. G. Slow Magnetic Relaxation in Intermediate Spin S = 3/2 Mononuclear Fe(III) Complexes. *J. Am. Chem. Soc.* **2017**, *139* (46), 16474−16477.
(98) Ge, N.; Zhai, Y.-Q.; Deng, Y.-F.; Ding, Y.-S.; Wu, T.; Wang, Z.-X.; Ouyang, Z.; Nojiri, H.; Zheng, Y.-Z. Rationalization of Single-Molecule Magnet Behavior in a Three-Coordinate Fe(III) Complex with a High-Spin State (S = 5/2). *Inorg. Chem. Front.* **2018**, *5* (10), 2486−2492.
(99) Pierloot, K. Transition Metals Compounds: Outstanding Challenges for Multiconfigurational Methods. *Int. J. Quantum Chem.* **2011**, *111* (13), 3291−3301.

https://doi.org/10.1021/acs.inorgchem.1c00214
Inorg. Chem. 2021, 60, 6480−6491